POAC'13
Espoo, Finland

Proceedings of the 22nd International Conference on
Port and Ocean Engineering under Arctic Conditions
June 9-13, 2013
Espoo, Finland

ICE EDGE DETECTION WITH DUAL-POLARIZED SAR DATA

M. Similä [1], F. Dinessen[2], N. E. Hughes[2], M. Mäkynen[1]

[1]Finnish Meteorological Institute, Helsinki, FINLAND

[2] Norwegian Meteorological Institute, Tromso, Norway

Abstract

We have investigated the discrimination power of dual-polarized SAR imagery in ice edge detection. The proposed approach relied largely on the use of HV-polarization imagery consisting of 10 dual-polarized RADARSAT-2 scenes acquired between 20 and 30 January 2010 over the Kara and Barents Seas. The approach utilized the SAR imagery and two SAR based parameters which were transformed using principal component analysis prior to the classification. An exceptional feature in the dataset was the effect of the atmospheric gravity waves on open sea. It was seen that in highly dynamic ice edge conditions the classification approach gave reasonable results if the incidence angle was smaller than 35 degrees, and in some cases also at higher angles. The resulting classification maps were compared to the OSI SAF sea ice edge product which gave consistent results with the SAR data.

1. Background

The location of the sea ice edge in the Arctic is needed in many applications, e.g. ship navigation, numerical weather, and sea ice models. Currently the operational sea ice edge products are derived from microwave radiometer data and, in some cases, using in addition scatterometer data. The major problem in obtaining the ice edge chart in this manner is that it has a relatively coarse resolution (10-20 km) (Steinwood 2011).

The RADARSAT-2 (RS-2) SAR has the capability to produce dual-polarized (HH and HV) ScanSAR images. Using a data set of 10 RS-2 dual-polarized ScanSAR Wide images acquired in January 2010 we have investigated the detection of the ice edge. The use of two polarizations reveals different properties of the target because they have varying sensitivities to the various characteristics of the sea ice surface and medium. The essential difference is that the HV-polarized radar response is a result of multiple scattering. The multiple scattering also explains why the strength of the backscattering coefficient at C-band HV-polarization (σ^o_{HV}) is typically less than one tenth of the σ^o_{HH} value which is dominated by single scattering (Onstott 1992). For both polarizations the surface roughness of ice and the structure of its top 5-20 cm layer governs the strength of the backscattering at C-band.

In this paper we first describe the data set including weather data and the preprocessing of the images. Then we briefly discuss the different SAR signature characteristics of open water and sea ice. Prior to the SAR classification we apply a principal component transform (PCA) to the SAR data and then we go through the different phases of the classification procedure. The classification results that were obtained are then discussed. Finally, we compare the

classification maps, as well as a visual interpretation of the SAR imagery, to the Ocean and Sea Ice Satellite Application Facility (OSI SAF) ice edge products.

2. Data

2.1 SAR Data

We acquired 10 RS-2 ScanSAR Wide dual-pol (HH and HV) images starting from 20 January and ending on 30 January 2010. The test area covered the southern Kara Sea between the Yamal Peninsula and Novaya Zemlya and the eastern part of the Barents Sea near Novaya Zemlya.The width of the images is 500 km and the nominal resolution is 100 m. The SAR preprocessing steps included rectification to polar stereographic projection with the latitude a 70^{o}N latitude of true scale and reference longitude of 63^{o}E, land masking, and compensation of the backscatter incidence angle variation. The nominal noise floor for the HV channel is around -28.5±2 dB and varying across the swath for all the antenna beams, and it is generally lower near the middle of the beam (Jeffries 2012). We ran a noise floor correction program provided by the Canadian Ice Service to eliminate the artifacts in the HV image induced by the antenna patterns. However, even after this correction the processed HV images were plagued by severe artifacts, e.g. the σ^o_{HV} level often changed drastically between different beams. Due to the large variation of the incidence angle in a single ScanSAR Wide scene (from 18 to 49 degrees) a nonlinear incidence angle correction was applied. The correction equations are based on the analysis of a large set of RS-2 HH and HV images. We first compute the value of the correction factor for the reference angle 31^o:

$$c^r_{HH}(31°) = 9.179 + (-1.0687 \cdot 31) + (0.01078 \cdot 31^2), \quad (1)$$

$$c^r_{HV}(31°) = -20.4477 + (-0.124 \cdot 31) + (0.00067 \cdot 31^2).$$

Then for the angle range [18,49] the correction factors are obtained from the curves:

$$c_{HH} = c^r_{HH} - \left(9.179 + (-1.0687\alpha) + (0.01078\alpha^2)\right), \quad (2)$$

$$c_{HV} = c^r_{HV} + (-20.447 + (-0.124\alpha) + (0.00067\alpha^2)).$$

where α refers to the incidence angle of the pixel. We note that this strongly decreases σ^o_{HH} at small incidence angles. After the incidence angle correction both HH and HV SAR images were despeckled using a median filter.

2.2 Weather and Sea Ice Conditions

During the test period wind speeds remained high (over 10 m/s, even reaching 20 m/s) almost all the time. There was a great variation in air temperatures during the same period, in the coastal weather station in the southern Kara Sea they ranged from -5 ºC to -25 ºC. Short periods of lower wind speeds were associated with cold air outbreaks. On the east coast of Novaya Zemlya the air temperatures were close to 0 ºC, because of the presence of open sea, but even there the wind speeds were often higher than 10 m/s.

Due to the strong winds our test area underwent a freezing process in highly dynamic circumstances. The ice extent had its maximum at the beginning of the test period (20 January), retreated up until 27 January, and then the ice edge started to advance again. The windy conditions kept the ice edge very fractured. Usually the ice edge - open water boundary consisted of brash ice or very small ice floes. There was also consolidated very thin new ice

areas, as well as brash ice bands broken away from the ice pack, drifting in open water in several SAR scenes.

3. SAR signatures from open water and sea ice

The marginal ice zone (MIZ) is the part of the sea ice cover sufficiently near to the open sea such that interactions with it result in modification of the ice properties. The penetration of waves and swells into the ice pack fractures it and the actual ice edge is usually a mixture of brash ice and slush. As the wave field moves further into the ice pack, the higher-frequency waves get damped and as a result, there is a systematic increase in the floe size as one moves deeper into the ice pack. The compactness of the ice pack is dependent on the wind direction, with the extreme cases being that wind is blowing normal toward ice (producing ice concentrations ~100 %) or that wind direction is away from ice pack (diffuse ice edge).
The radar backscattering from the open ocean is dominated by small capillary-gravity waves that are present on the surface of larger waves and swells. The occurrence frequency of these capillary-gravity waves depends on the wind speed. The MIZ is often associated with several oceanic and atmospheric phenomena which modify the small scale sea surface roughness (Wadhams 2000) and in our data set atmospheric gravity waves (Jacobsen 1999) manifested themselves particularly strongly. When the westerly winds blow above the mountains and hills of Novaya Zemlya the resulting atmospheric gravity waves cause large wind speed variations in the ocean surface at the scale of tens of kilometers. This phenomenon can be seen in a SAR image as highly oscillating σ^o patterns on the eastern side of Novaya Zemlya. We call these open water areas which are modulated by these atmospheric gravity waves "gravity wave areas". They complicate our open water/sea ice discrimination task and significantly affect our classification procedure.

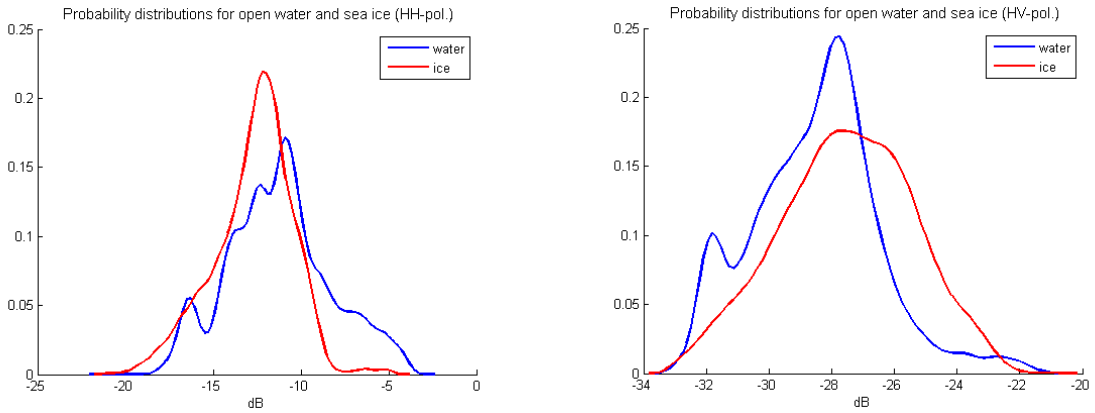

Figure 1. The probability distributions of σ^o for open water (blue color) and sea ice (red color) from the training data (HH left, HV right). There were totally 40,000 samples.

To describe the σ^o variation over open water and sea ice pack we selected three SAR images for our training data. From these images we chose several small windows which represented both relatively calm and windy wave conditions. The samples from within the ice pack consisted of thin new ice areas at different development stages, level ice fields, brash ice zones and small ice floes floating in the middle of a diffuse MIZ. The training sample set covered practically the whole σ^o variation range for both classes (Figure 1). We note that with the exception of brash ice most of the σ^o_{HH} values were concentrated on the range [-16, -11] dB and that the average σ^o_{HV} for sea ice is somewhat higher than for open water.

4. Classification

4.1 Principal component analysis

There are no persistent σ^o_{HH} or σ^o_{HV} patterns over the open water. In the 200 m image, resolution used in the classification, small scale surface features of sea ice (ridges, rafted ice, small open water areas between ice floes, cracks, narrow leads) characteristic of broken and deformed ice fields usually appear too blurred or the patterns are too incomplete to be discerned. The diversity and the ambivalence of σ^o_{HH} and σ^o_{HV} patterns led us to treat this classification problem focusing on the detection of open water areas and some numerical parameters were selected which were effective in this respect.

The first selected parameter was the depolarization ratio (Depol), which on the logarithmic scale equals the polarization difference HV-HH in dB. This value often helps to locate open water areas (Scheuchl 2004.). The homogeneity of the local σ^o_{HH} variation is described here as the difference between the maximum and minimum values inside a small image window (MaxMin). The values of this are typically small for open water and larger for sea ice, the latter property originating from deformation or fragmentation of ice cover. The variation of σ^o_{HH} and σ^o_{HV} is also rather small for undeformed fast ice and level ice fields. Usually the brash ice bands are narrow and their MaxMin has a high value. Of these parameters Depol was sometimes able to successfully identify even the problematic gravity wave areas. On the other hand, the MaxMin feature was not able to separate the gravity wave areas from sea ice areas.

Our feature vector for the detection of open water is (σ^o_{HH}, σ^o_{HV}, Depol, MaxMin). The addition of other features would have been possible, but the strong inherent noise present in the HV-channel would have forced us to compute the additional features in the HH-channel and then the relative importance of the HV-channel, the main issue of interest here, would have decreased. Hence, we restricted our attention to this 4-component feature vector where two of the components depend directly on σ^o_{HV} .

Although the feature vector is not large, the selection of the appropriate metric for the classification is problematic. To simplify this issue we performed a principal component analysis for the data where we computed the eigenvectors and the eigenvalues of the covariance matrix formed from the training data. Inspection of the proportion $\lambda_i / \sum \lambda_i$ where λ_i refers to the i^{th} eigenvalue, gives the fraction of the total variance accounted for by the principal component PC i. The first eigenvector gave largest weights to the features MaxMin and Depol and accounted for 42 % of the total variance. In the second eigenvector the largest weights were assigned to σ^o_{HH} and σ^o_{HV} (32 % of the variance). The third eigenvector also accounted for a considerable fraction of the variance (25%). The experiments showed that even if PC 3 is not insignificant, its inclusion in the classifier actually weakened the discrimination between open water and sea ice (probably due to the increased complexity when we moved from 2-d space to 3-d space in the classification metric). We restricted the PCA to the two first PC vectors explaining 74 % of the total variance.

4.2 Classification procedure

The naive Bayes classifier (NBC) is a probabilistic classifier based on applying the Bayes' theorem with strong (naive) independence assumptions (Domingos and Pazzani, 1997). The difference between the naive Bayesian classifier and the traditional Bayesian classifier is the following. The latter one can be written as

$$p(C|F_1,\dots,F_n) = \frac{p(C)p(F_1,\dots,F_n|C)}{p(F_1,\dots,F_n)} \qquad (1)$$

where C refers to the class, F_i the parameter vector PC i, and $p(C)$ is the prior probability for the classes. In the NBC we assume that the conditional parameters given the class are independent. Hence Eq. (1) simplifies into the product of the parameter densities given the class, i.e.,

$$p(C|F_1,\dots,F_n) = \frac{1}{Z}p(C)\prod_{i=1}^{n} p(F_i|C)$$

where Z is constant once the values of F_i (i.e. PC values) are known. The PC values are uncorrelated but not necessarily independent. In our training set the distributions $p(F_i|C)$ were highly non-gaussian and the needed distributions were estimated using the kernel estimator.

To make the classifier as sensitive as possible for the variation present in the different parameters we defined the effective range for each parameter prior to the computation of the PC transform. The applied effective ranges were: for σ^o_{HH} [-19, -8] dB, for σ^o_{HV} [-31, -24] dB, for MaxMin [0.7, 4] dB and for Depol [-17.5, -13] dB. The NBC worked well for the training data, giving just 12 % classification error for both classes. The decision regions are shown in Fig. 2. Despite the promising results for the training data, the pixelwise application of the NBC did not perform well for the rest of the SAR images.

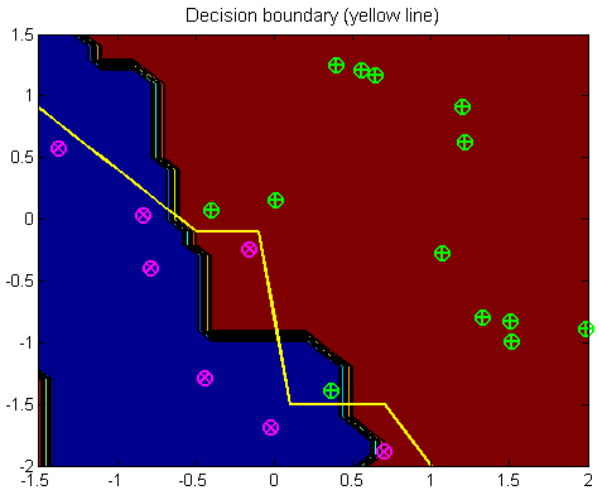

Figure 2. The decision boundary (yellow line) applied in the discrimination between open water. The red region corresponds the sea ice and the blue region open water according to the naïve Bayes classifier. The circled points refer to the cluster means (magneta for open water, green for ice), see text.

To improve the classification result we refined the discriminant boundary using sample means over a large sample set. This was performed by studying the distribution of cluster means in the PC 1 - PC 2 plane with the k-means clustering algrorithm. The k-means algorithm can be regarded as a deterministic variant of the EM-algorithm which approximates the distribution with a fixed number of gaussian components (Hastie et al. 2003). We varied the amount of clusters from 4 to 7 for each training image. Then we selected those cluster means which included only or mostly either open water or ice, see Fig. 2. At this phase we included in the training data some cluster means (4) that deviated essentially from the training data means, derived from two other SAR images. Together we had 20 cluster means when we subjectively fitted a decision boundary (yellow line) between the two classes. The classification was carried out in four sequential steps:

Step 1. We performed first the k-means clustering with 6 clusters for the whole image. Then we labeled the whole cluster to represent open water or ice according to the decision boundary. This usually resulted in a large numer of erroneously classified pixels.

Step 2. The MaxMin parameter is a measure of local σ^o_{HH} variation. We augment it with a gradient image that gives a structural information on this variation. The morphological gradient by Soille (2003) was applied with an empirically determined threshold. The areas of large gradients were extended to small segments using a morphological dilation operation. The inclusion of the gradient information improved the identification of ice cover. However, the gravity wave regions were often misinterpreted as ice on the basis of this criterion.

Step 3. a) Very low σ^o_{HH} (<-20 dB) jointly with very low σ^o_{HV} (<-30 dB) were interpreted as open water. These areas may in some cases have also contained nilas.

b) If Depol was smaller than -18.5 dB then the area was interpreted as open water. If Depol was less than -17.5 dB and σ^o_{HH} >-13 dB, the area is also classified as open water. This rule was applied independent of the step 2.

Step 4. Then the classification map was smoothed by a majority filter. Finally very small areas were removed with morphological operations (Pierre 1999).

5. Classification results

The image set was too small to give a highly reliable assessment about the performance of the proposed classification approach. We illustrate its performance with three examples. Figure 3 consists of a closed pack ice area in the Kara Sea, open water area modulated by the atmospheric gravity waves between Novaya Zemlya and pack ice, and an open water area in the Barents Sea. The closed ice pack area is classified correctly as is the open water area in the Barents Sea. The magnitude of Depol over the open sea decreases gradually as the incidence angle increases. At around an angle 35^o-40^o this discriminant is no longer an efficient open water identifier depending on the open water value of σ^o_{HH} (see Step 3b in the classification). The area between the compact ice pack and Novaya Zemlya comprised mainly of open water with some new ice areas and brash ice bands. This interpretation is supported by the Depol image. Because the gravity waves induce large wind speed variations on the surface, σ^o_{HH} and σ^o_{HV} for open water vary rapidly on the eastern side of Novaya Zemlya. This often leads to misclassification of open water as ice. Hence, the ice covered area between Novaya Zemlya and the compact ice pack is often overestimated.

In Figure 4 the SAR image covers approximately the same area as in the previous figure. The backscattering level from open sea is higher than in Figure 3. Loose ice bands and the

wind-scattered brash ice zone b form complex structures in the low ice concentration area and a locally large σ^o_{HH} and σ^o_{HV} variation between the compact ice pack and Novaya Zemlya. This results in an ice concentration overestimation on eastern side of Novaya Zemlya. The Depol image is strongly affected by the calibration problems in the HV image and this complicates its use as a discriminant.

In Figure 5 there is a fast ice area in the Pechora Sea (the lower left part of the SAR image). The backscattering statistics from fast ice were often very close to those from open water in both polarizations. Therefore the fast ice area was difficult to separate from open water area if the wind speed was high (over 10 m/s). The discrimination problem was particularly difficult at high incidence angles (>40^o) and resulted in misclassifications in the fast ice area.

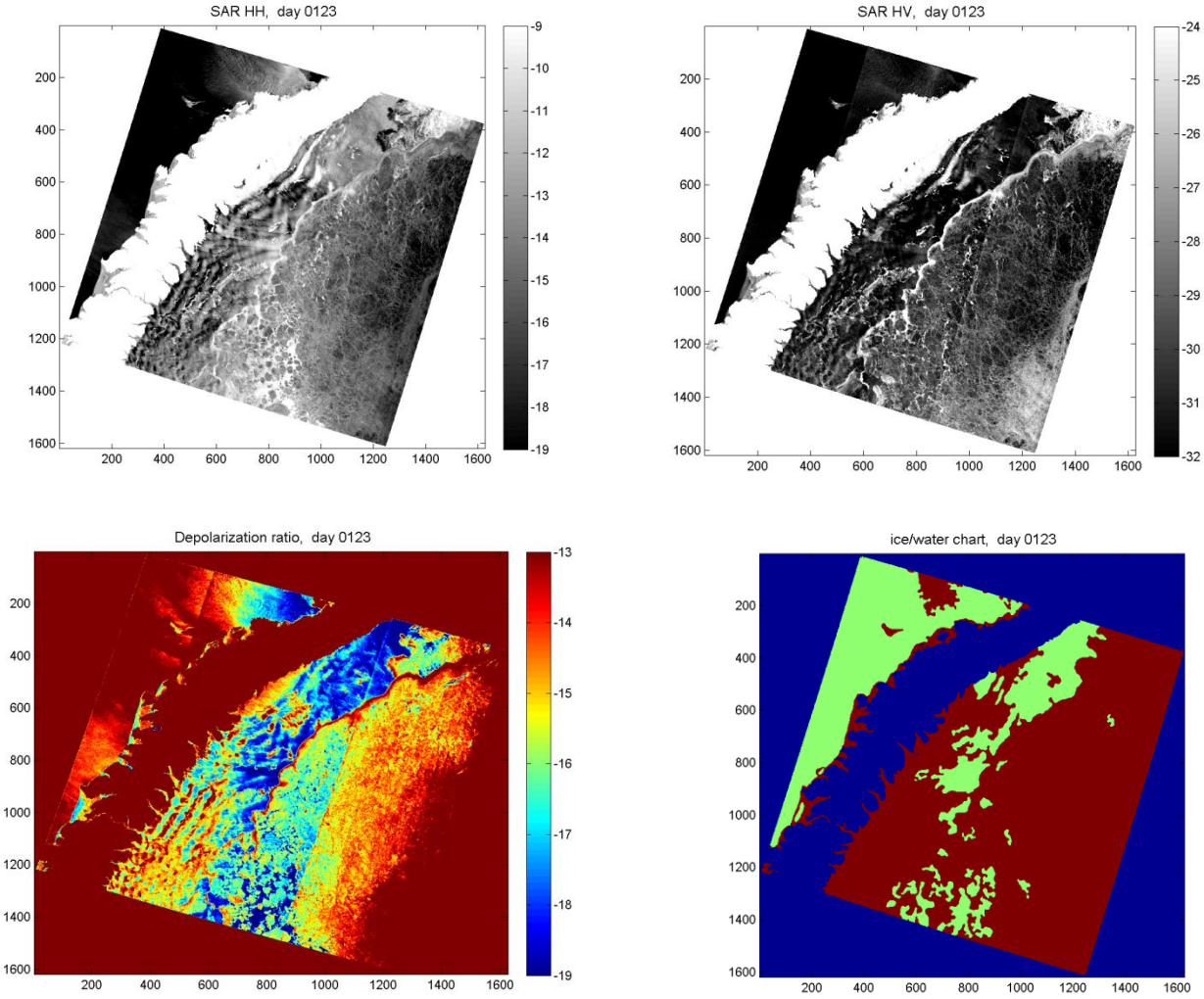

Figure 3. The RADARSAT ScanSAR Wide images acquired on 23 January 2010. In the upper panel are shown the HH- and HV-channels, respectively. In the lower panel is the depolarization image and the classification result (brown=ice, green=water). The incidence angle in the image ranges from 18 to 49 degrees.

The overall classification performance for our 5 training images and 5 test images can be regarded as acceptable when we consider that most of the errors are concentrated in the gravity wave areas and the fast ice area in the Pechora Sea. The occurrence of atmospheric gravity waves as well as the presence of fast ice at an ice edge rarely happens in the Arctic

seas. The locations of the errors suggest that the algorithm would very likely perform considerable better in more conventional circumstances. The SAR signatures from open water and sea ice varied significantly. The classification procedure yielded good results for training data images. Also the identification of the fast ice at high incidence angles was successful for these images, at least partly due to the relatively low σ^o_{HH} and σ^o_{HV} for open water. The retrieval of open water areas at very large incidence angles (> 45^o) usually had considerable difficulties.

The results for the test SAR images did not differ essentially from the training set in 3 of 5 cases. In two cases there occurred large erroneously interpreted regions. The majority of classification errors occurred at high incidence angles, over 40^o, and in both cases a significant fraction of the fast ice area in the Pechora Sea was misclassified as open water. In the test images there were also some difficulties in the classification of open water areas at high incidence angles, likely due to the backscatter values being close to the noise floor of the SAR images. In the gravity wave regions we systematically overestimated the magnitude of ice concentration.

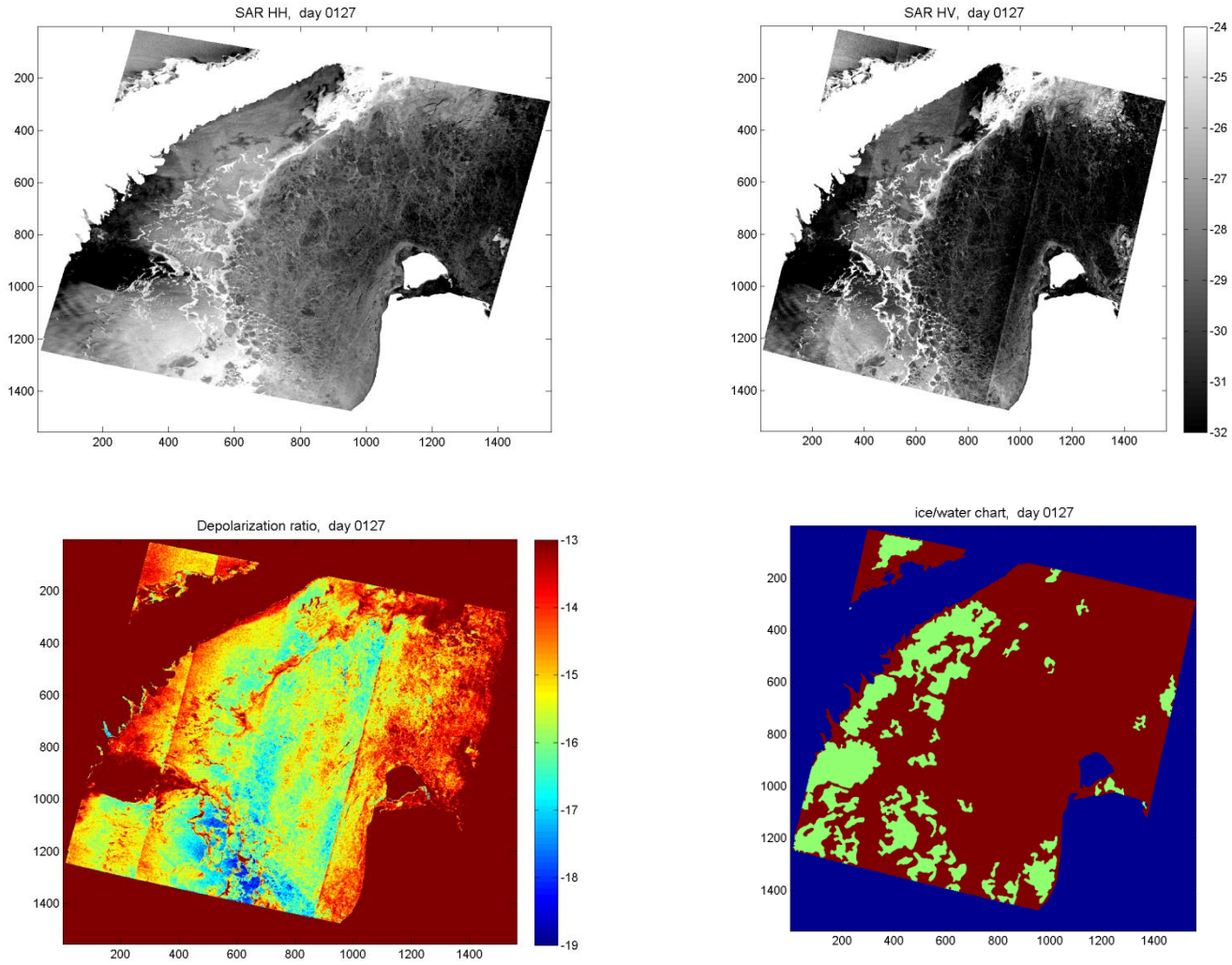

Figure 4. The RADARSAT ScanSAR Wide images acquired on 27 January 2010. In the upper panel are shown the HH- and HV-channels, respectively. In the lower panel are the depolarization image and the classification result (brown=ice, green=water).

6. Assessment of the OSI SAF ice edge product

In this section we briefly compare the SAR image and the automatic classification results to the OSI SAF ice edge product. The sea ice edge product is one of the operational sea ice products provided by the OSI SAF. The ice edge algorithm proceeds as follows. First, ice class probabilities (closed ice, open ice and water) are calculated based on SSM/I data at 19 GHz and 35 GHz. Then an analysis on the grid of 10 km is done using only SSM/I 85 GHz and ASCAT scatterometer data. The result is then filtered with the lower frequency SSM/I data (frequencies 19 and 35 GHz). The resulting ice edge chart is given in a 10 km grid although it's true resolution is lower. The different data sets are combined using a Bayesian approach (see details in Eastwood 2011). The ice in the OSI SAF i ice edge products is classified according to the ice concentration (IC): 0-34 % (water), 35-70 % (open ice) and > 70 % (closed ice).

In all 10 cases the OSI SAF ice edge product (IE) agrees well with the visual interpretation of the SAR images. The only minor differences are that some small new ice areas visible in the SAR data are classified in the IE product as open water, or some open water areas according to the SAR data are classified as open ice. The closed ice areas are practically the same for both data sets (±5-20 km). The good agreement between the SAR data and the IE product is illustrated in Figure 6. Due to cold weather and low winds open water areas are freezing. From the classification point of view the discrimination of open water and sea ice for dual-pol SAR image pair was much easier for Figure 5 than those ice conditions shown in Figures 3 and 4. It may be that some areas classified on the basis of SAR data as open water in Figure 5 were actually thin new ice.

We note that the IE product has good identification of the ice edge over the gravity wave areas. Those areas were difficult to classify using only the SAR data. It is likely that the IE product that contains information of regional IC is a more informative product than a SAR based binary classification map which leaves the quantification of IC for the user.

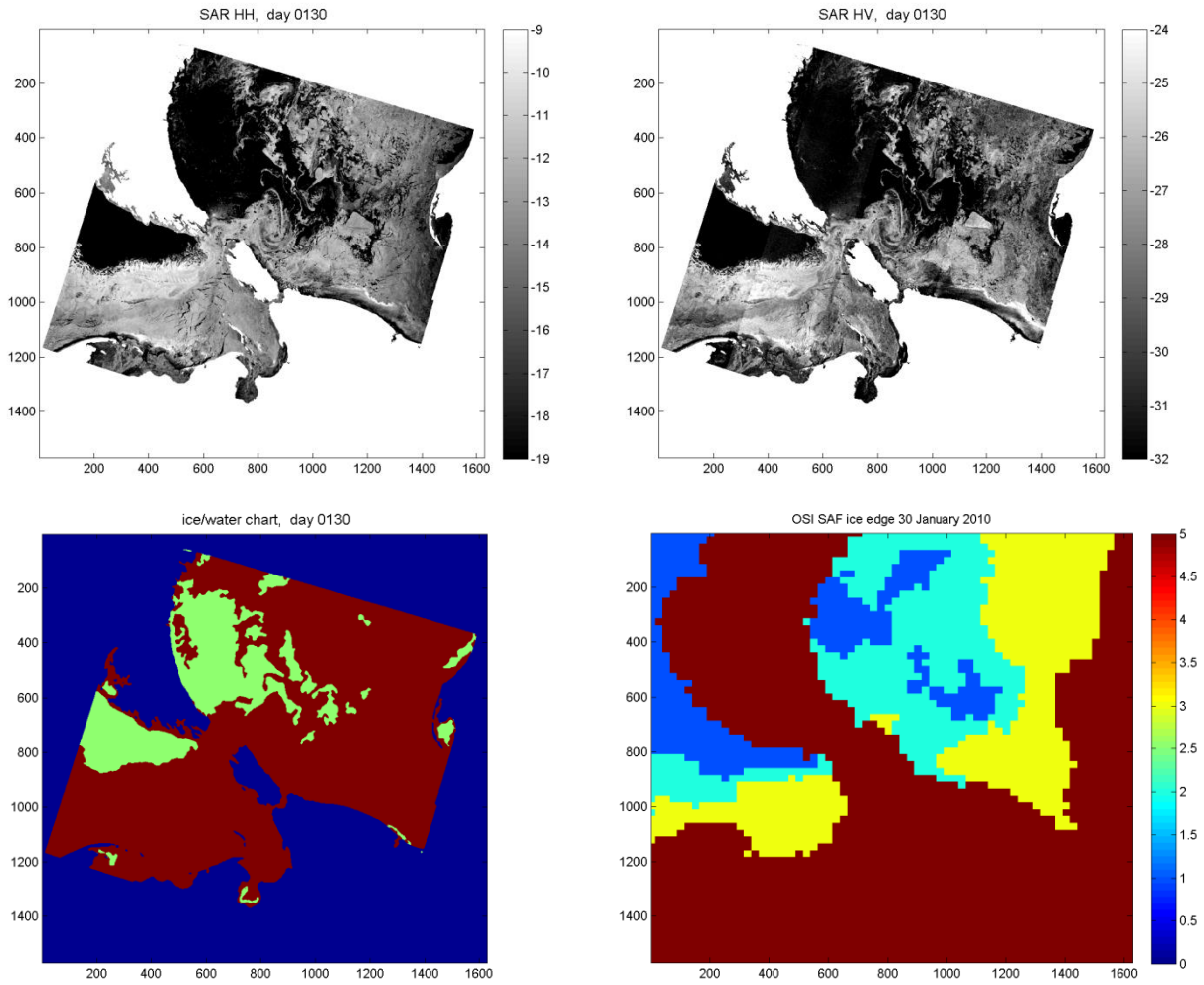

Figure 5. The RADARSAT ScanSAR Wide images acquired on 30 January 2010. In the upper panel are shown the HH- and HV-channels, respectively. In the lower panel is the classification result (left, brown=ice, green=water, blue=land) and the OSI SAF ice edge product (blue water, light blue=open ice, yllow=closed ice, brown=land). In the southernmost part of the images appears a fast ice area in the Pechora Sea. The brash ice areas in open water form eddy-like structures in southern Kara Sea (upper panel).

7. Conclusions

We have investigated the discrimination power of dual-polarized SAR imagery for ice edge detection. The proposed approach relied heavily on the use of the HV-polarization imagery. The limited amount of SAR images at our disposal (only 10 SAR images) prevents us making any conclusive assessments on the accuracy or the robustness of the proposed classification procedure. An exceptional feature was the effect of the atmospheric gravity waves on open sea. In the Arctic there are only few places where this phenomenon can occur. The presence of the gravity wave areas was somewhat unfortunate for our purposes because we were forced to modify our classification procedure to take into account this rare open water type.

It was seen that in highly dynamic ice edge conditions a classification approach utilizing dual-pol SAR imagery gave mostly reasonable results if the incidence angle was smaller than 35 degrees, and in some cases also at higher angles. At higher incidence angles the depolarization ratio (HV-HH in dB) was no longer reliable as a discriminant. The most problematic area for the classification was the fast ice area in the Pechora Sea. This is not, however, a serious limitation because fast ice areas seldom occur near the ice edge.

The comparison between the SAR based ice edge determination and the OSI SAF ice edge products showed that the OSI SAF product consistently yielded good results in the prevailing ice and weather conditions.

References:

Domingos P. and Pazzani M., 1997. "On the Optimality of the Simple Bayesian Classifier under Zero-One Loss", Machine Learning, 29, 103–130.

Eastwood, S. (ed.), 2011. Sea Ice Product Manual v. 3.7, Ocean and Sea Ice SAF documents, met.no, 35 pp.

Jacobson, M., 1999. Fundamentals of Atmospheric Modeling. Cambridge University Press, 656 pp.

Jeffries, B., 2012. "Radarsat 2 - New Ice Information Products", *International Ice Charting Working Group meeting*, Tromso, available from http://nsidc.org/noaa/iicwg/.

Hastie, T., R. et al., 2003. The Elements of Statistical Learning, Springer-Verlag, 533 pp.

Onstott, R.G., 1992. "SAR and scatterometer signatures of sea ice", Microwave Remote Sensing of Sea ice, F. D. Carsey (ed.), American Geophysical Union, pp. 73-104.

Scheuchl, B., D et al, 2004. **"**Potential of RADARSAT-2 data for operational sea ice monitoring**",** *Can. J. Remote Sensing*, 30(3), 448–461.

Soille, P., 2003. Morphological Image Analysis: Principles and Applications, 2nd Edition, Springer-Verlag, 408 pp.

Wadhams, P., 2000. Ice in the Ocean, Gordon and Breach Science, 351 pp.